THE EUROPEAN
PHYSICAL JOURNAL PLUS

Check for
updates

Transition path dynamics across rough inverted parabolic potential barrier

Hua Li[1], **Yong Xu**[1,2,a] , **Yongge Li**[1,3], **Ralf Metzler**[4]

[1] Department of Applied Mathematics, Northwestern Polytechnical University, Xi'an 710072, China
[2] MIIT Key Laboratory of Dynamics and Control of Complex Systems, Northwestern Polytechnical University, Xi'an 710072, China
[3] Center for Mathematical Sciences & School of Mathematics and Statistics, Huazhong University of Science and Technology, Wuhan 430074, China
[4] Institute for Physics & Astronomy, University of Potsdam, 14476 Potsdam-Golm, Germany

Abstract Transition path dynamics have been widely studied in chemical, physical, and technological systems. Mostly, the transition path dynamics is obtained for smooth barrier potentials, for instance, generic inverse-parabolic shapes. We here present analytical results for the mean transition path time, the distribution of transition path times, the mean transition path velocity, and the mean transition path shape in a rough inverted parabolic potential function under the driving of Gaussian white noise. These are validated against extensive simulations using the forward flux sampling scheme in parallel computations. We observe how precisely the potential roughness, the barrier height, and the noise intensity contribute to the particle transition in the rough inverted barrier potential.

1 Introduction

Rate theory [1] aims at providing a physical understanding of the long-time behaviour of systems, in which different "states" exist that are separated by barriers in the free energy landscape. These may be molecular systems, for instance, different molecules reacting with each other, or (such as proteins) individual molecules with different conformations. Other systems may be biological or technical. The different states are locally stable. In order to make a "transition" from one state to another, an energetic barrier needs to be crossed. This process is typically fuelled by thermal energy, and the involved barrier is considerably larger than $k_B T$, where k_B is the Boltzmann constant and T the absolute temperature. As a consequence, the barrier crossing typically requires many attempts, corresponding to a rare successful event. This latter statement is embodied in the famed Arrhenius law for chemical reactions, stating that the rate of a reaction is proportional to the Boltzmann factor for the "activation energy", $k \propto \exp(-E_a/[k_B T])$ [2]. An important step towards the calculation of absolute transition rates (i.e. including the prefactor A in the expression for the rate, $k = A \exp(-E_a/[k_B T])$) was the formulation of transition state theory, pioneered by the two complementary approaches of Eyring [3] (a "thermodynamic approach" [4]) and Wigner [5] (a "classical mechanics approach" [6]). A kinetic approach to rate laws was provided by

---

[a] e-mail: hsux3@nwpu.edu.cn (corresponding author)

 Springer

Kramers' seminal work relating rate theory with Einstein's and Smoluchowski's theory of Brownian motion [7–9]. For details, we refer to the review article by Hänggi, Talkner, and Borkovec [10].

The sampling of transition state dynamics is vastly hampered by the above-mentioned fact that the system spends most of the time vibrating in a locally stable state, while the transition itself is a rare event. Experimentally, single-molecule spectroscopy provides unprecedented insights into the individual transition paths of molecular reactions [11–15]. Similarly, single-molecule force spectroscopy techniques were shown to resolve transition path kinetics [16–18]. In computer simulations of transition paths, a naive simulation of the process (e.g. in protein folding) cannot provide sufficient statistics for the rare transition events in standard computing times. Groundbreaking new sampling methods, originally developed by Chandler and coworkers [19,20], have by now become standard repertoire in chemical physics [21–24].

Concretely, the "transition path" describes "direct" crossing times from an "entry point" to an "exit point" of the transition state located at specific energy surfaces. Here, "direct" means that only such paths are considered that will not take the system back to the entry point, but successfully transition from entry-to-exit point or vice versa. Remarkably, there exists a time reversal symmetry between the entry–exit and exit–entry paths [20,23,24]. This equivalence was extended to the full distributions of crossing times, for instance, for the translocation times in membrane channel crossing processes [25]. The transition path properties have attracted much attention also in protein and nucleic acids folding reactions [26–28]. Understanding the statistical information of transition paths is thus of vital importance for chemical reactions [10] and is at the heart of modern transition state theory [29]. As the transition paths capture the real transition time during direct crossing events, they are fundamentally different from the first-passage paths which could be obtained from implementing reflecting and absorbing boundaries for the transition region, respectively, as first-passage paths include all those "indirect" events, that repeatedly take the system back to its original state [30]. In fact, the distinction between direct and indirect paths is similar to the distinction of direct and indirect trajectories in the theory of first-passage time statistics in which direct paths correspond to the geometry-control in the probability density of first-passage times [31–34]. In chemical reactions, this geometry-control superimposed to the reaction-control reflects the barrier crossing to successful reaction [35–37].

Mathematically, a transition path can be derived from implementing two absorbing boundaries at the extreme points of the transition region (i.e. the entry and exit points) [38]. Thus, trajectories that are absorbed at the opposite end of the transition region with respect to the initial condition are transition paths, while those that are absorbed at the same boundary are looping paths [39]. As first-passage times count both kinds of paths, transition path times (TPTs) [40] are necessarily shorter than the corresponding first-passage times. In addition to the TPT, the "transition path velocity" (TPV) and transition path shapes are important quantities for the description of transition path properties. The TPV is the ratio of the interval length dx of the transition path to the time spent in this interval. In contrast to the TPT, the TPV directly characterises the speed of the particle transition [41]. In turn, the transition path shape is a characteristic of the dynamic profile of the time versus the position of the particle in the transition region [42].

Recently, a number of studies have concentrated on the TPT, the TPV, and the transition path shape based on theoretical, experimental, and simulations approaches. For a Markov process, these quantities were studied in the context of protein folding landscapes [43], generic parabolic barriers [44,45], double well linear cusp potentials [46], or a harmonic ramp [47]. It was shown that the results can be derived from the forward or backward Fokker–Planck equation [48]. In non-Markovian activated rate processes, the TPT could also be obtained

theoretically [45,49–52]. Interestingly, the symmetry of the TPT between entry–exit and exit–entry transitions becomes broken when coloured noise is driving the activation process [53].

The potential functions considered in these studies are all *smooth*. In reality, however, the potential function is often characterised through significant roughness, a phenomenon occurring widely in biology, chemistry, physics, and engineering. Examples include transitions in transmembrane helices [54], complex liquids, and materials close to the glass transition [55,56], the energy landscape of proteins and RNA molecules [57], to name but a few. Hence, the study of the properties of transition paths in rough potentials is of practical significance. For such cases, the choice of a smooth potential mimicking the reaction barrier is overly idealised for the convenience of solving the dynamic equations. Indeed, the roughness of energy landscapes affects a series of dynamic behaviours. Thus, it was shown to give rise to dramatic effects on particle diffusion [58] and transport [59,60], folding and binding reactions [61], escape times [60,62] and rates [63,64], as well as the position of the maximum current [65]. Therefore, the effect of a rough potential barrier on transition paths properties is an important case for further studies. We emphasise here that adding roughness into the potential function of the system is equivalent to adding a nonlinear force term. Since the solution of the properties of the transition path involves the solution of the Fokker–Planck equation, even the simple inverted parabolic potential function selected in this article is difficult to solve for analytical results of the transition path properties, and therefore numerical approaches become important. The major idea of this study is the analysis of numerical schemes in comparison with (approximate) theoretical solutions of the rough barrier crossing problem.

Here, we consider four central statistical quantities characterising the transition dynamics, namely, the mean TPT, the TPT distribution, the mean TPV, and the mean transition path shape in a generic, one-dimensional inverted parabolic potential with superimposed roughness, under the driving of Gaussian white noise. Specifically, by means of a spatial averaging approximation, theoretical results for the four statistical observables are presented. Moreover, we consider the influence of barrier height and noise intensity on the properties of the transition paths and their delicate interplay with the roughness parameters. We analyse in detail the numerical schemes and compare the numerical results with analytical approximations of the barrier crossing dynamics. In particular, we also demonstrate the role of the spatial binning. In our simulations of this problem, as the barrier height increases the simulation of the mean TPT, the TPT density, the mean TPV, and the mean transition path shape involves sampling of rare events [66]. Here, we apply the forward flux sampling scheme [67] allowing for parallel computing and obtain simulations results for the four statistical quantities. In Sect. 2, we present the approximate theoretical results for the mean TPT, the TPT density, the mean TPV, and the mean transition path shape of particles in the rough inverted parabolic potential. In Sect. 3, we discuss the forward flux sampling scheme in detail, before applying it to verify the approximate theoretical results of the different quantities in detail in Sect. 4. Our conclusions are drawn in Sect. 5.

2 Transition path time and velocity distribution

We consider the mean TPT, the TPT density, the mean TPV, and the mean transition path shape in a rough inverted parabolic potential function under the driving of Gaussian white noise. The system can be described by the Langevin equation
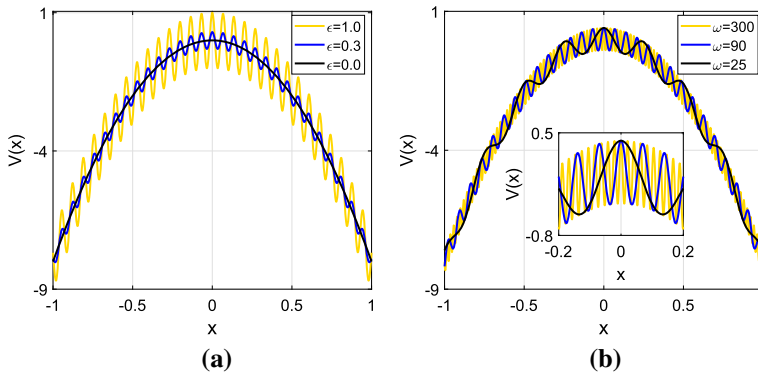
Fig. 1 Barrier potential $V(x)$ consisting of an inverted parabolic potential with superimposed sinusoidal "roughness" with amplitude ϵ and periodicity ω, $k = 16$, for different parameters: **a** $\omega = 93$ with different ϵ; **b** $\epsilon = 0.4$ with different ω

$$\frac{\mathrm{d}x}{\mathrm{d}t} = f(x) + \xi(t), \tag{1}$$

where x is the particle position, $f(x) = -\mathrm{d}V(x)/\mathrm{d}x$ is the force on the particle defined through the rough potential $V(x) = V_0(x) + V_1(x)$, in which $V_0(x) = -kx^2/2$ is the inverted parabola and $V_1(x) = \epsilon \sin(\omega x)$ represents the roughness in the Zwanzig sense [58]. The barrier shape factor k controls the height of the barrier, and the parameters ϵ and ω control the roughness $V_1(x)$. $V(x)$ changes with ϵ and ω as shown in Fig. 1. Due to the existence of the roughness term in the potential $V(x)$ features local minima and maxima. The number of maxima of $V(x)$ in the interval is related to the period ω of $V_1(x)$. Moreover, ϵ affects the height of the local barriers. Finally, in Eq. (1) $\xi(t)$ represents Gaussian white noise with covariance $\langle \xi(t)\xi(s) \rangle = 2D\delta(t-s)$ and the noise strength D. The noise ξ is the formal derivative of the Wiener process $W(t)$, that is, $\xi(t) = \mathrm{d}W(t)/\mathrm{d}t$.

2.1 Transition path time distribution

For our analytical derivations, we will use the Fokker–Planck equation corresponding to the stochastic Eq. (1) [68],

$$\frac{\partial P(x,t)}{\partial t} = -\frac{\partial}{\partial x}[f(x)P(x,t)] + D\frac{\partial^2}{\partial x^2}P(x,t). \tag{2}$$

Here, $P(x,t)$ is the probability density function of x. The probability current $J(x,t)$ is determined by the following equation,

$$J(x,t) = f(x)P(x,t) - D\frac{\partial}{\partial x}P(x,t). \tag{3}$$

We impose two absorbing boundaries at the entry and exit points x_A and x_B of the transition interval, such that $P(x_A,t) = P(x_B,t) = 0$. In the following, we take $x_A = -1$ and $x_B = 1$. Then, the TPT density $\rho_{x_B}(t)$ of the particles in the transition region from point x_A to x_B can be obtained from the current $J(x,t)$ near the point x_B [69],

$$\rho_{x_B}(t) \propto \lim_{\epsilon_0 \to 0} J(x_B + \epsilon_0, t). \tag{4}$$

The key to obtain the theoretical solution for $\rho_{x_B}(t)$ is to derive $P(x, t)$ from Eq. (2). However, in the rough potential $V(x)$ the roughness term $V_1(x)$ represents a nonlinearity. Therefore, even when $V_1(x)$ is added to a simple parabolic potential function, it is difficult to derive the exact theoretical solution of $P(x, t)$. Therefore, we need to find a way to deal with the roughness term. We choose the spatial averaging technique [58,70]. This approach changes the potential in the stochastic Eq. (1) into an effective potential and diffusion coefficient [58]

$$V^*(x) = V_0(x) + \log[I_0(\epsilon)] = -kx^2/2 + \log[I_0(\epsilon)], \tag{5a}$$

$$D^* = D/I_0^2(\epsilon), \tag{5b}$$

where $I_0(x)$ is the modified Bessel function and $\log(x)$ is the logarithm of base e. An approximate theoretical solution of $\rho_{x_B}(t)$ may then be written in the form [69]

$$\rho_{x_B}(t) = \frac{D^*kx_B}{2[1 - \mathrm{erf}(x_B\sqrt{k/2})]}\sqrt{\frac{k}{\pi}}\frac{\exp[-kx_B^2/2\coth(kD^*t/2)]}{\sinh(kD^*t/2)\sqrt{\sinh(kD^*t)}}. \tag{6}$$

Here, $\mathrm{erf}(x) = (2/\sqrt{\pi})\int_0^x \exp(-s^2)\mathrm{d}s$ is the error function, and $\coth(t)$ and $\sinh(t)$ are the hyperbolic cosine and sine functions, respectively.

2.2 Mean transition path time

Based on the spatial averaging of $V_1(x)$, according to [71] an approximate theoretical solution of the mean TPT $\langle t_{TP}\rangle$ for the rough inverted parabolic function can be derived in the form

$$\langle t_{TP}\rangle = \frac{\int_{x_A}^{x_B} \exp(-\beta G(s))\int_s^{x_B} \exp(\beta G(x))\mathrm{d}x \int_{x_A}^s \exp(\beta G(x))\mathrm{d}x\,\mathrm{d}s}{D^* \int_{x_A}^{x_B} \exp(\beta G(s))\mathrm{d}s}, \tag{7}$$

where $V^*(x) = \beta G(x)$ and $\beta = 1/D^*$ are the quantities from Eqs. (5a) and (5b). In particular, in the low barrier limit [72],

$$\langle t_{TP}\rangle = \frac{\pi[\lambda(\mathrm{erf}(\alpha)^2 - 1)\mathrm{erfi}(\alpha) + \mathrm{erf}(\alpha\lambda)]}{2D^*k\lambda\mathrm{erf}(\alpha)}, \tag{8}$$

where $\alpha = \sqrt{k/2}$, $\lambda = \sqrt{\pi^2/8 - 1}$ and $\mathrm{erfi}(x) = 1 - i\,\mathrm{erf}(ix) = \frac{2}{\pi}\int_0^x \exp(-s^2)\mathrm{d}s$ is the imaginary error function.

2.3 Transition path velocity

Next, we consider the mean TPV of particles in the transition interval $[x_A, x_B]$. Without the roughness, Eq. (2) can be transformed into the Smoluchowski equation [68]

$$\frac{\partial}{\partial t}P(x, t) = \frac{\partial}{\partial x}\left(D\exp\left(-\frac{G(x)}{D}\right)\frac{\partial}{\partial x}\exp\left(\frac{G(x)}{D}\right)P(x, t)\right), \tag{9}$$

with $V(x) = G(x)/D$. According to Eq. (9), the probability density function $P_{TP}(x, t)$ of transition paths is described by (see 1)

$$\frac{\partial}{\partial t}P_{TP}(x, t) = \frac{\partial}{\partial x}\left(D\phi_B^2(x)\exp\left(-\frac{G(x)}{D}\right)\frac{\partial}{\partial x}\frac{\exp(G(x)/D)}{\phi_B^2(x)}P_{TP}(x, t)\right), \tag{10}$$

where $\phi_B(x)$ is the "committor function". Specifically, $\phi_B(x)$ is the solution of the system of equations [73]

$$L\phi_B(x) = 0, x \in (x_A, x_B),$$
$$\phi_B(x_A) = 0,$$
$$\phi_B(x_B) = 1. \tag{11}$$

Here, $L = \frac{\partial}{\partial x} V(x) \frac{\partial}{\partial x} - D \frac{\partial^2}{\partial x^2}$ is the backward Fokker–Planck operator [68,73].

From Eq. (11), we find that

$$\phi_B(x) = \frac{\int_{x_A}^{x} \exp(\beta G(s)) \, ds}{\int_{x_A}^{x_B} \exp(\beta G(s)) \, ds}. \tag{12}$$

Hence, the mean TPV $\langle v_{TP}(x) \rangle$ is given by [72]

$$\langle v_{TP}(x) \rangle = D \frac{d\phi_B(x)/dx}{\phi_B(x)[1 - \phi_B(x)]}. \tag{13}$$

Therefore, the combination of Eqs. (12) and (13) yields

$$\langle v_{TP}(x) \rangle = D \frac{\int_{x}^{x_B} \exp(\beta G(s)) ds}{\int_{x}^{x_B} \exp(\beta G(s)) ds \int_{x_A}^{x} \exp(\beta G(s)) ds} \exp(\beta G(x)). \tag{14}$$

Considering now the roughness, we apply a spatial averaging procedure to Eq. (1), to transform the rough inverted parabolic potential into the smooth counterpart. Equations (12) and (14) then become

$$\phi_B(x) = \frac{1}{2} \left(1 + \frac{\mathrm{erf}(\sqrt{k/2}x)}{\mathrm{erf}\left(\sqrt{k/2}x_B\right)} \right),$$
$$\phi_A(x) = 1 - \phi_B(x) = \frac{1}{2} \left(1 - \frac{\mathrm{erf}\left(\sqrt{k/2}x\right)}{\mathrm{erf}\left(\sqrt{k/2}x_B\right)} \right), \tag{15}$$

and

$$\langle v_{TP}(x) \rangle = \frac{4D^* \sqrt{\frac{\beta k}{2}} \mathrm{erf}\left(\sqrt{\frac{\beta k}{2}}x_B\right) \exp\left(-\frac{1}{2}\beta k x^2\right)}{\sqrt{\pi} \left[\mathrm{erf}^2\left(\sqrt{\frac{\beta k}{2}}x_B\right) - \mathrm{erf}^2\left(\sqrt{\frac{\beta k}{2}}x\right)\right]}. \tag{16}$$

2.4 Transition path shape

We proceed to the mean transition path shape of the particles in the rough inverted parabolic potential as presented in Fig. 1. Let $\tau_{shape}^{TP}(x_0|x_A)$ denote the mean shape of the transition path trajectories, where x_0 is a given mid-point in the transition region (x_A, x_B). This quantity can be calculated from the Fokker–Planck equation of the system. For the transition region $[x_A, x_B]$ with its absorbing boundary conditions at either interval limit, $\tau_{shape}^{TP}(x_0|x_A)$ is in fact identical to the mean first-passage time $\tau^{FPT}(x_A|x_0)$ of particles from the point x_0 to reach x_A, that is, we have the relationship [46]

$$\tau_{shape}^{TP}(x_0|x_A) = \tau^{FPT}(x_A|x_0), \tag{17}$$

and $\tau^{FPT}(x_A|x_0)$ in our system governed by Eq. (1) can be obtained by Dynkin's formula [73].

Similarly, after the spatial averaging process the mean first-passage time of particles from the point x_0 to x_A for the rough case is [47]

$$\tau^{\mathrm{FPT}}(x_A|x_0) = C\frac{\phi_B(x_0)}{\phi_A(x_0)} \int_{x_0}^{x_B} \exp(-V^*(x))\phi_A^2(x)\mathrm{d}x$$
$$+C \int_{x_A}^{x_0} \exp(-V^*(x))\phi_A(x)\phi_B(x)\mathrm{d}x. \qquad (18)$$

Analogously, the mean first-passage time of particles from point x_0 to x_B reads

$$\tau^{\mathrm{FPT}}(x_B|x_0) = C\frac{\phi_A(x_0)}{\phi_B(x_0)} \int_{x_A}^{x_0} \exp(-V^*(x))\phi_B^2(x)\mathrm{d}x$$
$$+C \int_{x_0}^{x_B} \exp(-V^*(x))\phi_A(x)\phi_B(x)\mathrm{d}x, \qquad (19)$$

where we used the abbreviation $C = \int_{x_A}^{x_B} \exp(-V^*(x))\mathrm{d}x = \sqrt{2\pi/k} \times \mathrm{erf}(\sqrt{k/2}x_B)$ $I_0(\epsilon)/D^*$, and $\phi_A(x), \phi_B(x)$ are the same as in Eq. (15). With these expressions, the mean transition path shape $\tau^{\mathrm{TP}}_{\mathrm{shape}}(x_0|x_A)$ can be calculated from Eqs. (17) to (19).

Simultaneously, the quantity $\tau^{\mathrm{TP}}_{\mathrm{shape}}(x_0|x_A)$ can also be derived from the statistic of particle transition trajectories. In transition paths simulations, that is, we obtain $\tau^{\mathrm{TP}}_{\mathrm{shape}}(x_0|x_A)$ as the average

$$\tau^{\mathrm{TP}}_{\mathrm{shape}}(x_0|x_A) = \sum_{i=1}^{m} \sum_{j=1}^{N_i} \frac{\tau^{\mathrm{TP}}_{ij}(x_0|x_A)}{N}. \qquad (20)$$

Concretely, that is, we measure the mean transition path shape of m transition path segments from x_A to x_B. During this process, the transition path segment may cross the point x_0 multiple times. According to Eq. (20), $\tau^{\mathrm{TP}}_{\mathrm{shape}}(x_0|x_A)$ is then obtained as the double sum over the $\tau^{\mathrm{TP}}_{ij}(x_0|x_A)$, the period that the particle crosses x_0 for the jth time in trajectory i. N_i denotes the cumulative number of times that the particle crosses x_0 in the ith transition path. Finally, $N = N_1 + N_2 + \cdots + N_m$ is the total number of crossings through x_0 for all m transition paths (Fig. 2).

3 Simulations setup using the forward flux sampling scheme

For our simulations, we apply the forward flux sampling scheme [67] to obtain the mean TPT, the TPT density, the mean TPV, and the mean transition path shape. Taking the calculation of mean TPT as an example, we briefly introduce the simulation process, and the calculation of other quantities is analogous. In Fig. 3, for transition paths crossing the interval $[x_A, x_B]$ we insert a series of disjoint interfaces $\lambda_0, \lambda_1, \lambda_2, \cdots, \lambda_n$ in this transition interval. Simulating M_i times for each interface separately, the time spent in each interface region was obtained. Here, the particle will start from interface λ_0, and we stop the simulations when the particle reaches the interface λ_1, or when it returns to interface λ_0. After repeated simulations on interface λ_0 for M_i times, we record the time the particles spend in this interval. For the simulation on the interval $[\lambda_i, \lambda_{i+1}]$, we let the particle start from the interface λ_i and stop the simulation when the particle reaches the next interface λ_{i+1} or returns to interface λ_0. In the simulation process on this interval, we allow the particle to return to the previous interfaces but not to the initial interface λ_0. Similarly, we record the time the particles spend in this interval.
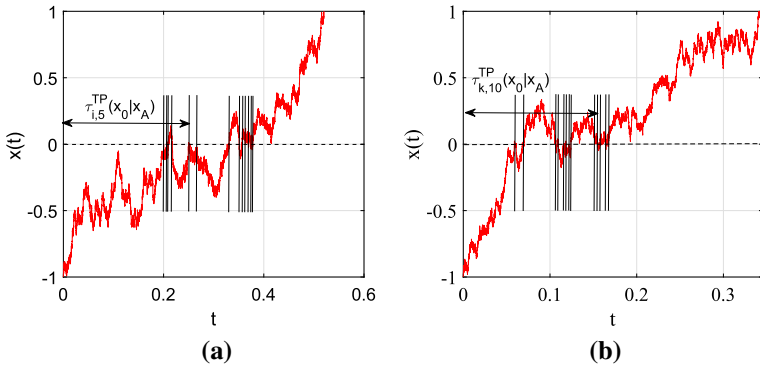
Fig. 2 Two transition sample paths i and k in the rough invited parabolic potential from entry point $x_A = -1$ to exit point $x_B = 1$. Evidently, the transition path crosses the point $x_0 = 0$ repeatedly. We record the instants $\tau_{ij}^{TP}(x_0|x_A)$ when the transition path crosses x_0 to calculate the transition path shape $\tau_{shape}^{TP}(x_0|x_A)$ from x_A to x_0 according to Eq. (20). In the two panels, $j = 5$ for sample path i and $j = 10$ for sample path k

Fig. 3 Schematic of the forward flux sampling method. We define a series of interfaces λ_i in the interval $[x_A, x_B]$. The "paths" from interface λ_i to λ_{i+1} are successful paths which do not return back to the entry point-interface λ_0
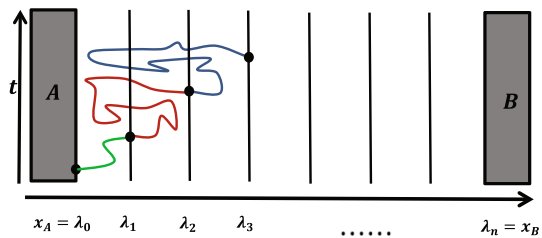
In order to speed up the simulations, the particles may simultaneously start from each interface, such that we can employ parallel computing schemes. The simulation stops when the particle reaches the next interface or returns to the initial interface. These steps are repeated multiple times at all interfaces, and we record the time consumption of the particles in the transition path intervals during this simulation procedure. Then, we sum the time of the particles recorded in each interval to obtain the transition time of the particles in the entire transition path interval. Therefore, in this scheme we shift the simulation of the entire transition path interval to a simulation process within a series of small intervals. In the following, we use $n = 400$ interfaces.

4 Transition path time statistic across rough inverted parabolic potential

We now employ the simulations scheme to analyse the mean TPT, the TPT density, the mean TPV, and the mean transition path shape of a particle in a rough inverted parabolic function under the driving of Gaussian white noise. Effects of the noise intensity of the driving noise, the roughness amplitude, and periodicity are explored. We compare the simulations results with the approximate theoretical results, observing good agreement.

4.1 Transition path time distribution

Figures 4 and 5 show our results for the TPT density $\rho_{x_\mathrm{B}}(t)$ for different parameters, along with the analytical result (6). In particular, we examine the influence of the noise strength D in panel 4a. As expected, shorter transition times become more emphasised for higher D. Concurrently, the TPT distribution narrows somewhat, so that the most probable value increases with D. Conversely, the TPT density shifts towards longer times and becomes broader with increasing rough parameter ϵ, as shown in panel 4b. The local barriers imposed by the superimposed roughness lead to an appreciable slow-down of the transition times. In the presence of roughness in the potential function, as shown in Fig. 1, the local maxima of the transition region increase, and the time required for particles to leave these local maxima increases, as well, and therefore also the TPT of particles in the whole transition region. In other words, the roughness in the inverted parabolic potential function impedes the transition of particles in the transition region $[-1, 1]$. A similar phenomenon is shown in Fig. 6b. This is in contrast to the effect of the noise intensity D and barrier height k on $\rho_{x_\mathrm{B}}(t)$. We note that as the magnitude of ϵ increases, the accuracy of the approximate theoretical result worsens, especially around the most likely transition times. Figure 4c displays the variation of the TPT density with the barrier height, given in terms of the barrier shape factor k. This parameter obviously has a major effect. For increasing barrier height (increasing k), the TPT density shifts to *shorter* TPT values and becomes more concentrated. This a priori counterintuitive behaviour stems from the fact that the TPT is a conditional process. While barrier crossing becomes increasingly rare for higher barriers the duration of the rare successful events becomes faster.[1] Concurrently, the first-passage time, that considers both successful and unsuccessful crossing attempts, will increase with increasing k and compare the discussion of Fig. 6 below. This effect is, of course, quite similar for situations with and without roughness. Note also that for higher barriers the agreement with the theoretical result (6) is improved. Finally, panel 4d shows the TPT density for different roughness periodicity ω. As can be seen, the effect is quite minor. Apparently, it does not matter whether the system features a larger or smaller number of local minima, within the examined parameter values.

Subsequently, we considered the influence of the noise intensity D and the barrier height k on $\rho_{x_\mathrm{B}}(t)$ for different roughness parameters ϵ. As shown in Fig. 4e, f, the peak value $\max(\rho_{x_\mathrm{B}}(t))$ of the TPT density increases with growing D or k. However, for different ϵ the degree of growth is different. Specifically, as ϵ increases, $\max(\rho_{x_\mathrm{B}}(t))$ increases slowly with increasing D or k. Compared with the case of $\epsilon = 0$, the influence of D and k on the $\rho_{x_\mathrm{B}}(t)$ is less for the rough potential case.

To gain more insight into the exact behaviour of the one-sided TPT density, we analyse its shape in the short- and long-time limits, $t \to 0$ and $t \to \infty$. For short t, Eq. (6) reduces to

$$\rho_{x_\mathrm{B}}(t) \sim \frac{x_\mathrm{B}}{1 - \mathrm{erf}\left(x_\mathrm{B}\sqrt{k/2}\right)} \frac{\exp(-x_\mathrm{B}^2/[D^*t])}{\sqrt{\pi D^* t^3}}. \tag{21}$$

We note that the partial expression $x_\mathrm{B}(\pi D t^3)^{-1/2} \exp(-x_\mathrm{B}^2/[D^*t])$ here is exactly the Lévy–Smirnov short-time form of the first-passage time density in a semi-infinite domain, in which the distance to the absorbing boundary is x_B. The exponential cutoff reflects the fact that the diffusing particle needs a finite time to cover the distance x_B [31,32,35,36,76]. Taking the

---

[1] Compare this situation with the variation of the mean first-passage time in piecewise linear potentials in [74,75].
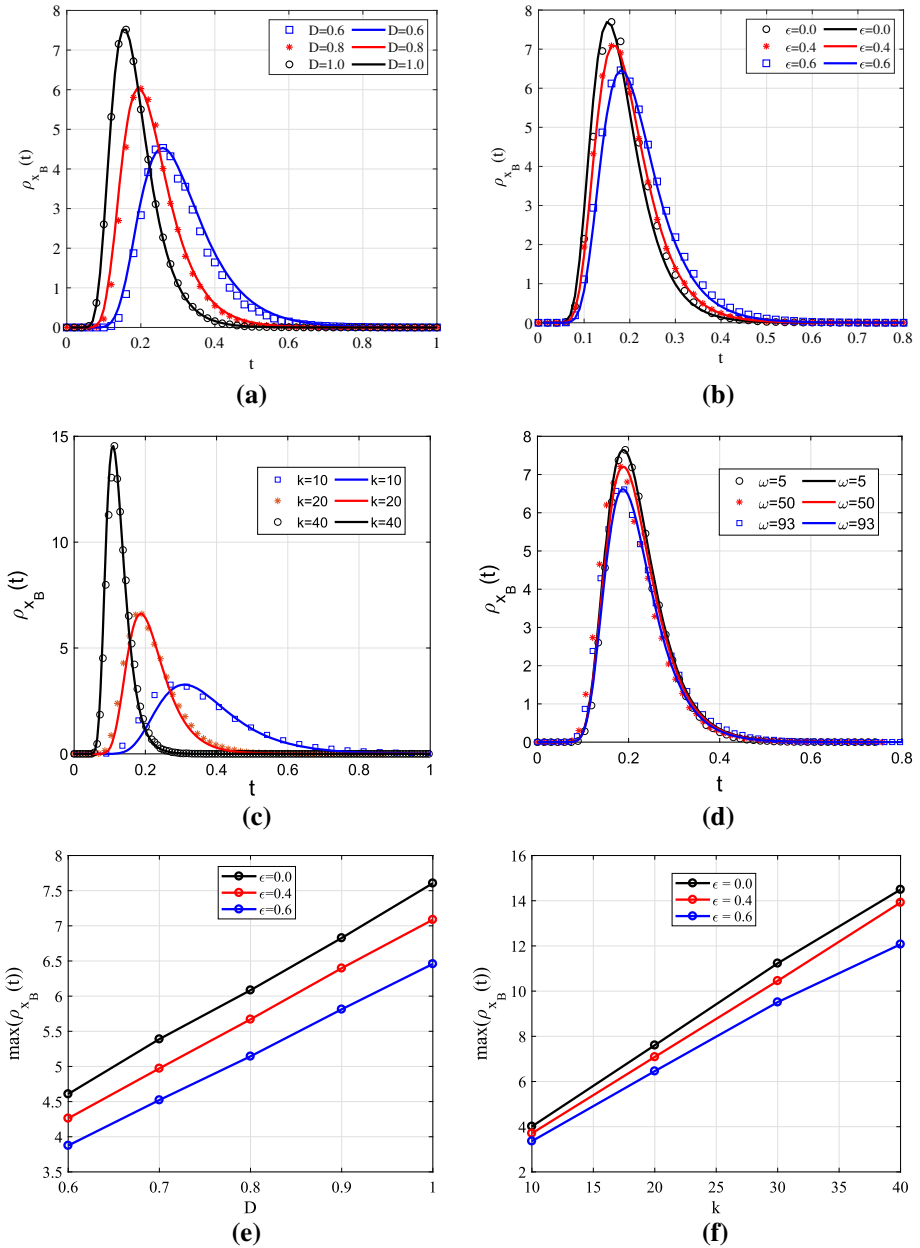
Fig. 4 TPT density as function of time for various parameters. **a** Different noise strengths D for $k = 20$, $\epsilon = 0.2$, and $\omega = 93$. **b** Different roughness amplitudes ϵ for $k = 20$, $D = 1$, and $\omega = 93$. **c** Different barrier shape factors k of the inverted parabolic potential, for $D = 1$, $\epsilon = 0.2$, and $\omega = 93$. **d** Different roughness periodicity ω, for $k = 20$, $D = 1$, and $\epsilon = 0.2$. In Fig. 4a–d, the theoretical result (6) is shown by the full lines. Finally, we show $\max(\rho_{x_B}(t))$ for different roughness amplitudes ϵ for **e** $k = 20$ and $\omega = 93$, as well as **f** $D = 1$ and $\omega = 93$. The graphs in panels 4e, f are theoretical results from Eq. (6).

logarithm in expression (21),

$$
-\log(\rho_{x_B}(t)) \sim \frac{x_B^2}{D^*t} - \log\left(\frac{x_B}{(\pi D^* t^3)^{1/2}\left[1 - \mathrm{erf}\left(x_B\sqrt{k/2}\right)\right]}\right), \tag{22}
$$

such that the leading behaviour of $-\log(\rho_{x_B}(t))$ is given by the inverse power-law

$$
-\log(\rho_{x_B}(t)) \sim \frac{x_B^2}{D^*t}. \tag{23}
$$

At short times, we thus have the exponentially suppressed law $\rho_{x_B}(t) \sim \exp(-x_B^2/[D^*t])$. Remarkably, the barrier shape factor k only appears in the error function in the short-time expansion (21).

In the opposite limit of long t, Eq. (6) has the asymptote

$$
\rho_{x_B}(t) \sim \sqrt{\frac{2k}{\pi}} \frac{D^* k x_B}{1 - \mathrm{erf}\left(x_B\sqrt{k/2}\right)} \frac{\exp(-k x_B^2/2)}{\exp(k D^* t)}, \tag{24}
$$

and thus

$$
\log(\rho_{x_B}(t)) \sim \log\left(\sqrt{\frac{2k}{\pi}} \frac{D^* k x_B}{1 - \mathrm{erf}\left(x_B\sqrt{k/2}\right)}\right) - \frac{k}{2}x_B^2 - k D^* t. \tag{25}
$$

The leading behaviour is then

$$
\log(\rho_{x_B}(t)) \sim -k D^* t, \tag{26}
$$

that is, an exponential shoulder $\rho_{x_B}(t) \sim \exp(-k D^* t)$ at long times. Again, this exponential decay is analogous to the first-passage time density in a finite domain [31,32,35,36,76]. However, the main difference in result (24) is the Boltzmann factor-like suppression $\propto \exp(-k x_B^2/2)$ reflecting the barrier crossing process.

Figure 5 analyses the short- and long-time behaviour of the TPT density for a given set of noise strength D, for different barrier shape factors k and roughness parameter ϵ. As seen in panel 5a, the exponential suppression following from Eq. (23) is nicely fulfilled for all k. Figure 5c demonstrates how for increasing t (smaller values of $1/t$) deviations from this exponential suppression become visible, especially for $k = 40$. The exponential long-time behaviour encoded in expression (26) is nicely corroborated in Fig. 5b. Figure 5d shows the crossover behaviour around the most likely value. Finally, the exponential long- and short-time behaviour for different ϵ are shown in Fig. 5e, f, respectively. The exponential decay is more significant for larger ϵ. Also, at these intermediate times the description by the approximate theory shows a very good match.

4.2 Mean transition path time

We now explore the effects of barrier height, noise intensity, and roughness parameter ϵ on the mean TPT of the particles. Figure 6a demonstrates the decrease in the mean TPT with increasing noise strength D, which is expected. However, as before the mean TPT *decreases* with *increasing* barrier height, which is due to the construction of the TPT. The fact that this conditional time corresponds to increasingly rare events for growing k is corroborated by panel 6e, in which we show the corresponding mean first-passage time. The quantity t_{FPT} counts the overall time to cross the barrier, including unsuccessful attempts. As we see, the mean first-passage time *increases* with *increasing* k, in accordance with intuition. As shown
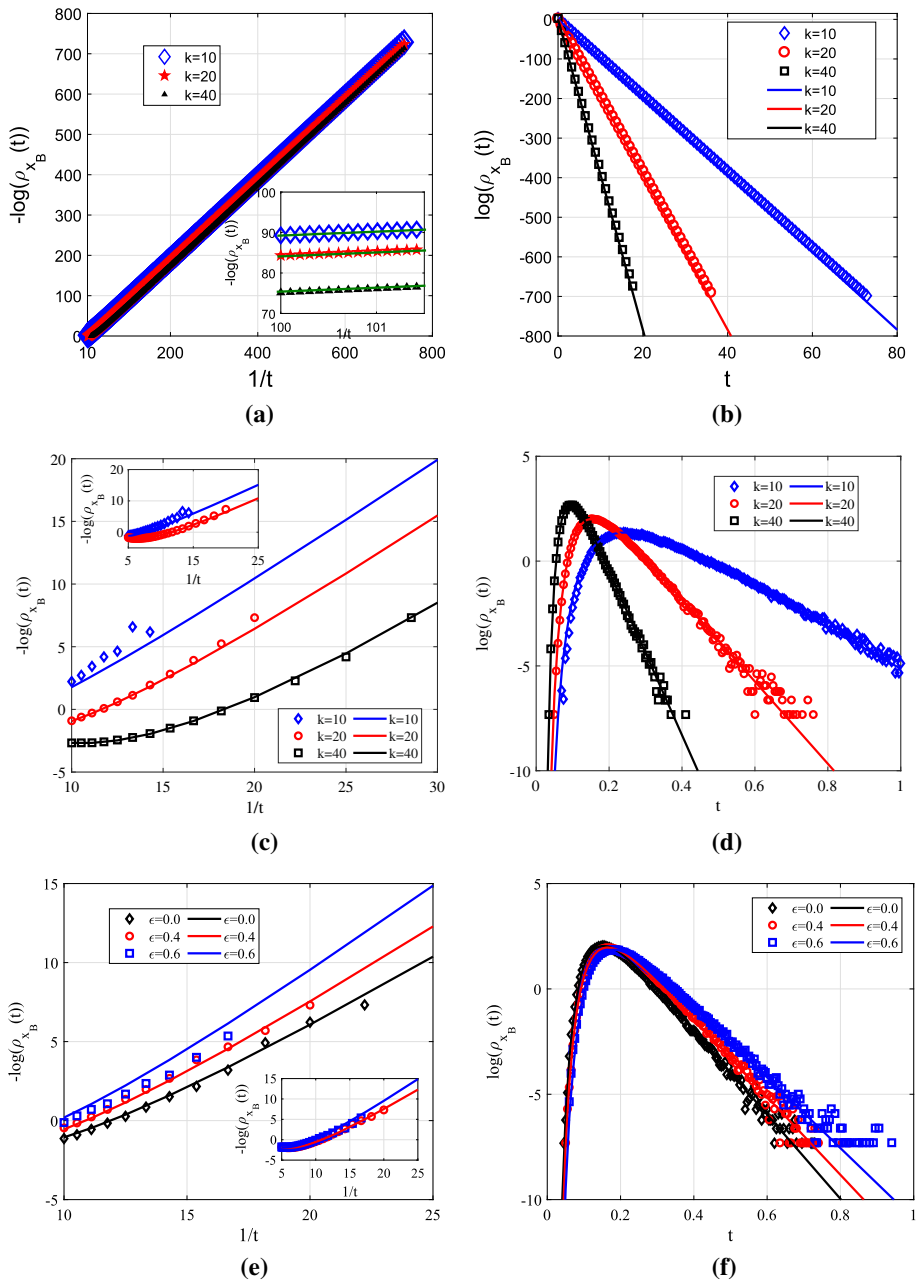
Fig. 5 TPT density for different barrier heights determined by the barrier shape factor k. The fixed parameters are $D = 1.0$, $\epsilon = 0.2$, and $\omega = 93$. **a** Short-time exponential suppression following Eq. (23). **b** Long-time exponential decay following Eq. (26). The symbols shown in **a** and **b** are results from Eq. (6), the lines in **b** represent expression (25). The slope of the green line in the inset of panel **a** equals x_B^2/D^*, following result (23). We observe nice agreement. Panels **c**–**f** shows simulations results (symbol) along with the behaviour encoded in Eq. (6). In panel **c**, **e**, we see that for increasing times (smaller values of $1/t$) deviations are visible, especially for $k = 40$ and $\epsilon = 0.0$. Panel **d**, **f** demonstrates that the crossover behaviour at intermediate times is nicely reproduced by expression (6)
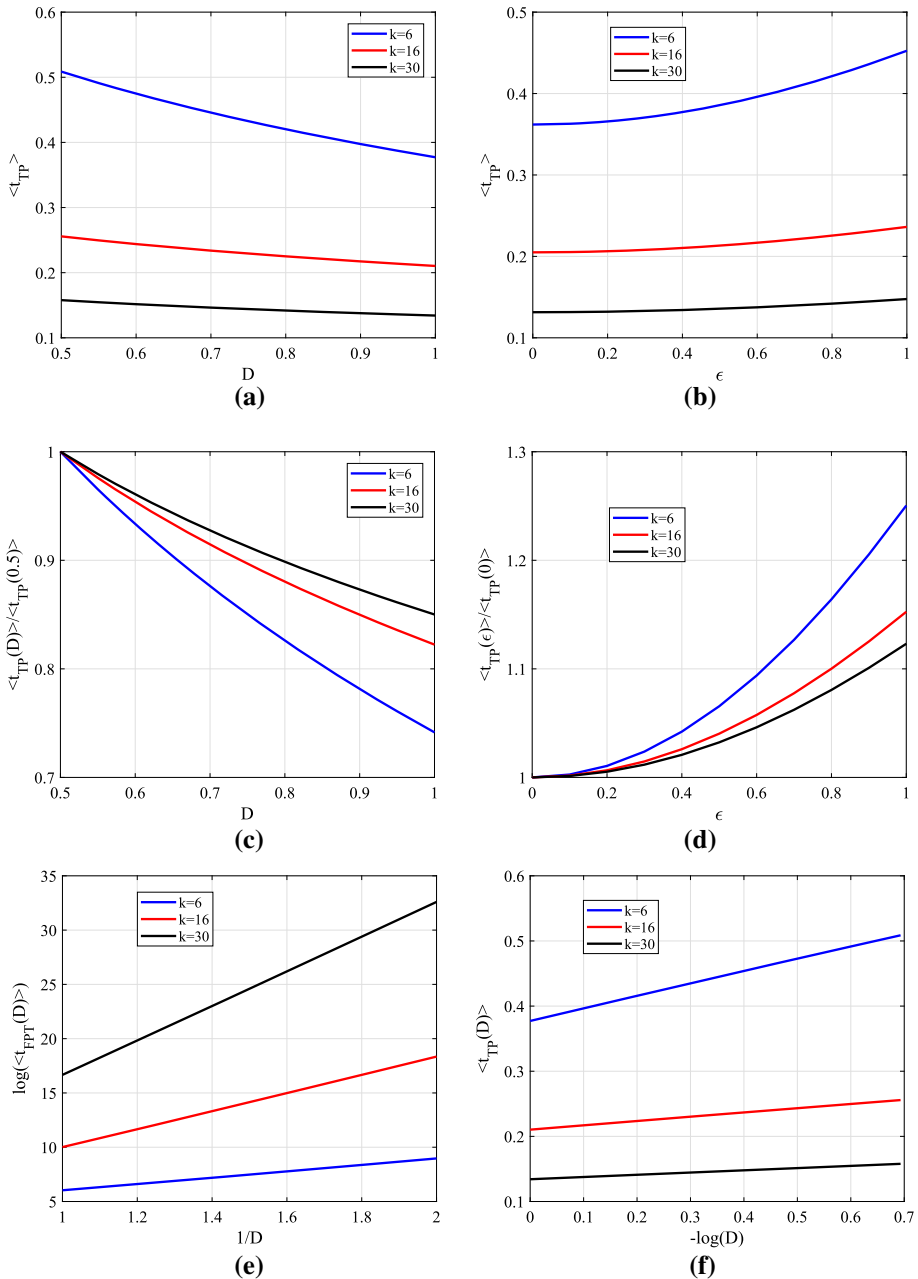
Fig. 6 Mean TPT for different barrier shape factors k. **a** Mean TPT as function of the noise strength D and for roughness amplitude $\epsilon = 0.4$. **b** Mean TPT as function of ϵ, for $D = 1$ and $\omega = 279$. **c** Ratio $\langle t_{\mathrm{TP}}(D) \rangle / \langle t_{\mathrm{TP}}(0.5) \rangle$ of the mean TPT normalised to the value at $D = 0.5$, as function of D. **d** Ratio $\langle t_{\mathrm{TP}}(\epsilon) \rangle / \langle t_{\mathrm{TP}}(0) \rangle$ normalised to the value at vanishing noise ($\epsilon = 0$), as function of ϵ. **e** Plot of $\log(\langle t_{\mathrm{FPT}}(D) \rangle)$ versus $1/D$. **f** Plot of $\langle t_{\mathrm{TP}}(D) \rangle$ versus $-\log(D)$ according to Eq. (7). The mean FPT corresponds to Eq. (27), and the mean TP is obtained from Eq. (7).

in panel 6b, the roughness promotes an increase in the mean TPT, and the effect becomes more pronounced for lower barrier heights (smaller k values). As shown in panels 6c and d, the effect of varying D and ϵ is, relatively, more pronounced at lower barrier heights (smaller k).

The influence of the roughness of the inverted parabolic potential on the mean first-passage time can be obtained from spatial averaging over the transition region $[x_A, x_B]$,

$$\langle t_{FTP} \rangle = \frac{1}{D^*} \int_{x_A}^{x_B} \exp(\beta G(x)) \int_{x_A}^{x} \exp(-\beta G(s)) \mathrm{d}s \mathrm{d}x, \tag{27}$$

where $\beta G(x) = V^*(x)$, $x = x_A$ is chosen as a reflecting boundary, and $x = x_B$ is an absorbing boundary. According to [73],

$$\langle t_{FTP} \rangle = K \exp(\Delta V/D^*), \tag{28}$$

where $\Delta V = V^*(x_A) - V^*(x_0)$, and K is a prefactor. Taking the logarithm,

$$\log(\langle t_{FTP} \rangle) \sim \Delta V/D^*. \tag{29}$$

Consequently, the slope of the lines shown in Fig. 6e is $k I_0^2(\epsilon)/2$ (see definition 5b).

The exact expression for the mean TPT directly follows from Eq. (7) in the form

$$\langle t_{TP} \rangle = \frac{\int_{x_A}^{x_B} \exp(V^*(x)/D^*) \left[\mathrm{erf}^2 \left(\sqrt{k/(2D^*)} \right) - \mathrm{erf}^2 \left(\sqrt{k/(2D^*)}x \right) \right] \mathrm{d}x}{\mathrm{erf} \left(\sqrt{k/(2D^*)} \right)}. \tag{30}$$

For barrier heights $\Delta G > 2k_B T$, the argument in [26] leads to the approximation (up to a constant prefactor)

$$\langle t_{TP} \rangle \sim \frac{K \log(2e^r \Delta V/D^*)}{2\pi}, \tag{31}$$

where $r = 0.577....$ is Euler's constant. As function of D^*, that is, we have the approximate proportionality

$$\langle t_{TP} \rangle \sim -K \log(D^*). \tag{32}$$

Therefore, through D^* ϵ affects the slope of the lines in Fig. 6e, f.

We finally show results for the mean TPT and the mean first-passage time for particles in the rough inverted parabolic potential with $k = 0.2$, as functions of the roughness amplitude ϵ. As shown in Fig. 7a, b, the variation with ϵ is well captured by the theoretical predictions, with a small deviation developing for increasing roughness. Note that in both panels the vertical axes correspond to the values normalised to the respective values at $\epsilon = 0$. With the increase in ϵ, the local maxima increase in the transition region, which is equivalent to the increase in meta-stability in this transition region. The time for particles to leave these meta-stable states in this transition region increases. Therefore, both the mean first-passage time and the mean TPT increase gradually in the transition region. In Fig. 7c, d, we consider the change of the mean TPT with barrier height k and noise intensity D for different roughness parameter ϵ. It is found that the mean TPT decreases with the increase in k or D. And with the increase in ϵ, the decreasing trend is gradually intensified. It also shows that the existence of the rough potential increases the influence of the barrier height and noise intensity on the mean TPT.
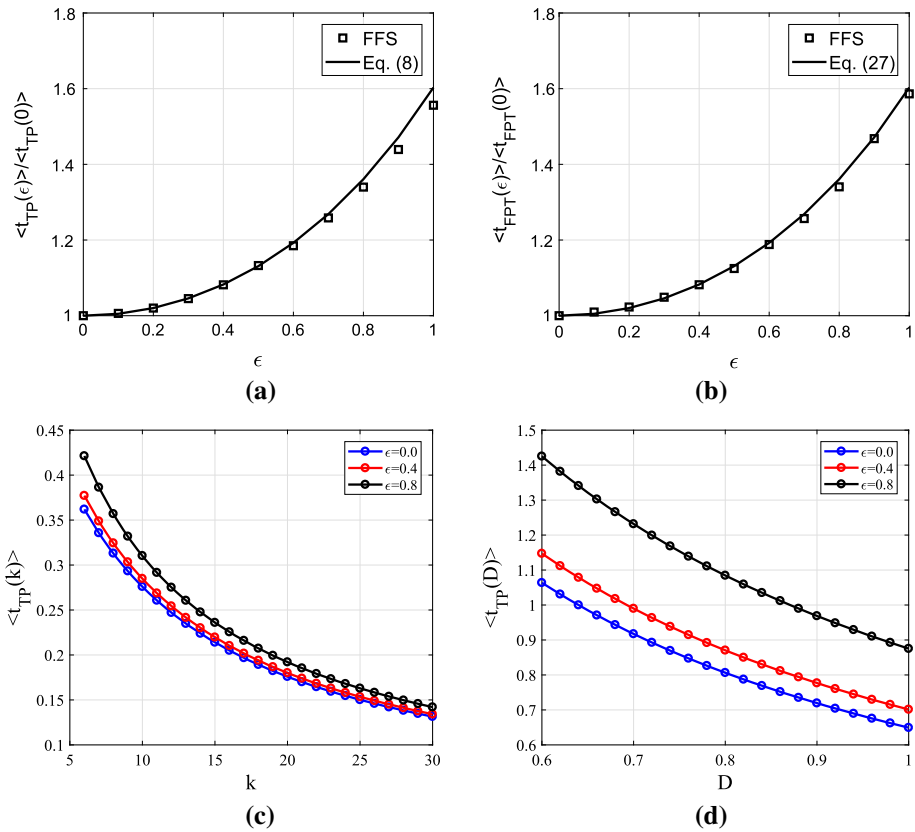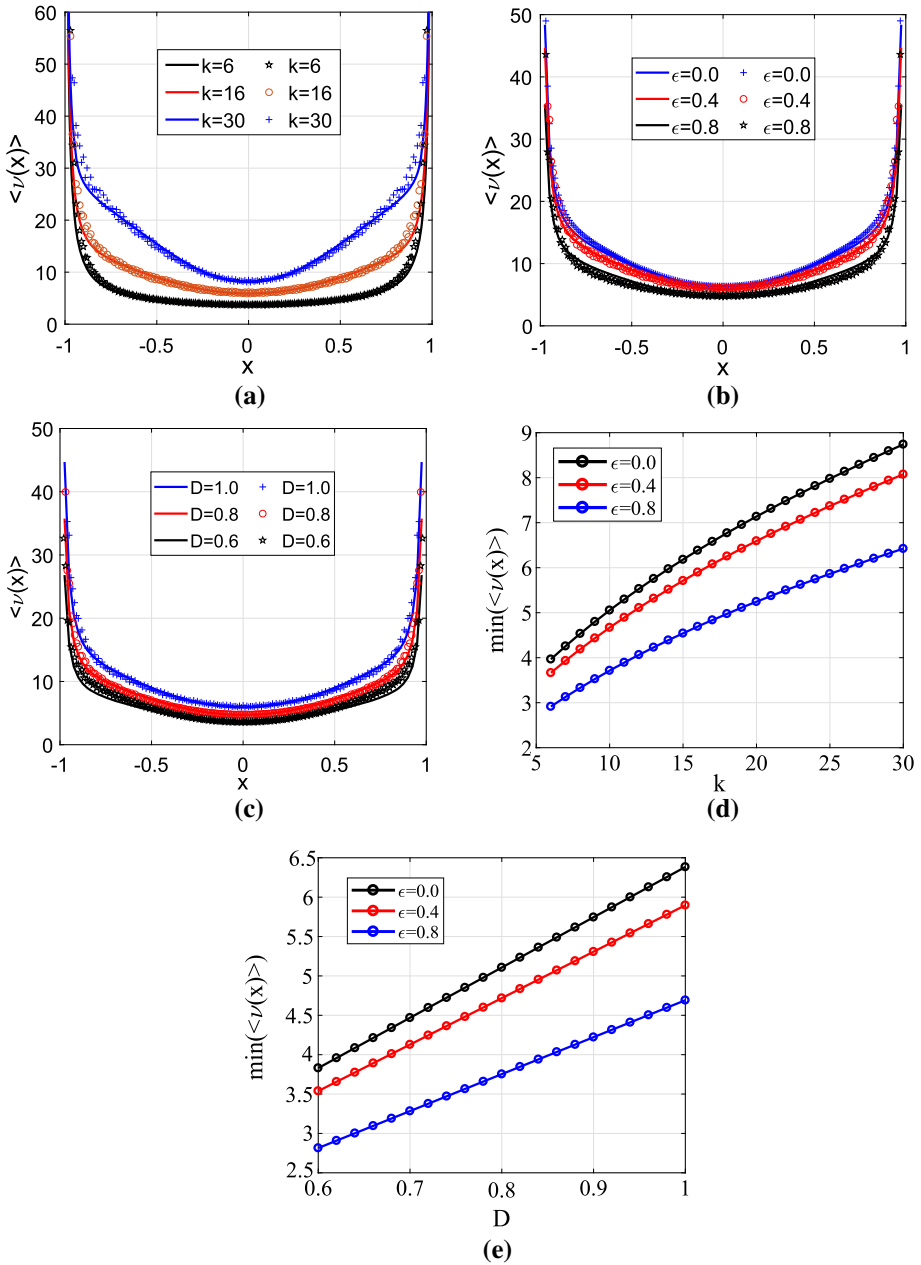
Fig. 7 **a** Mean TPT as function of roughness amplitude ϵ. **b** Mean first-passage time versus as function of ϵ. Both functions are normalised to the respective values at $\epsilon = 0$. The symbols represent results from the forward flux sampling scheme, lines are the theoretical results according to Eqs. (8) and (27), respectively. The barrier shape factor is $k = 0.2$. Mean TPT with different roughness amplitudes ϵ for **c** $D = 1$ and $\omega = 93$. **d** $k = 0.2$ and $\omega = 93$. In Fig. 7**c**, **d**, we show theoretical results from Eq. (8).

4.3 Mean transition path velocity

We now turn to the mean TPV and its dependence on the system parameters. The results are shown in Fig. 8. During the barrier crossing, the particles spend relatively more time in the flatter vicinity of the potential maximum at ($x = 0$) in the transition region. Correspondingly, at this maximum of the barrier potential the mean TPV of particle will have a minimum. As mentioned above, the TPT of particles is symmetric around the point $x = 0$ for particles traversing the transition region from entry point x_A to exit point x_B and in the opposite direction [25]. For this reason, the mean TPV is symmetric about the point $x = 0$. Furthermore, it can be seen from result (16) that the mean TPV will diverge at the two boundaries of the transition region $[-1, 1]$.

The mean TPV for three barrier heights is shown in Fig. 8a as function of the position x in the transition region. As the barrier height increases, the value of the mean TPV also increases, for all positions x. For the highest barrier in the panel, the behaviour changes to a significantly more pronounced V-shape around $x = 0$. The tendency to higher TPVs is

Fig. 8 Mean TPV $\langle \nu(x) \rangle$ as function of position x in the transition region $[-1, 1]$, for different **a** barrier shape factor k and $D = 1$, $\epsilon = 0.4$, $\omega = 279$; **b** noise strengths D and $k = 16$, $\epsilon = 0.4$, $\omega = 279$; **c** roughness amplitudes $\epsilon = 0.4$ and $k = 16$, $D = 1$, $\omega = 279$. Results from simulations are shown by symbols, the lines correspond to Eq. (16), as shown in Fig. 8a–c. $\min(\langle \nu(x) \rangle)$ with different roughness amplitudes ϵ for **d** $D = 1.0$ and $\omega = 93$; **e** $k = 16$ and $\omega = 93$. In Fig. 8d, **e**, the theoretical results from Eq. (16) are shown

in line with our observations above, according to which the transition is faster for higher barriers, due to the conditional monitoring of successful transition events, compare Fig. 6a. We note that while the agreement with the theoretical prediction (16) is very good, a slight deviation emerges for increased barrier height. In Fig. 8b, we examine the mean TPV for different noise intensities. As expected, a higher noise intensity leads to increased values of the mean TPV, in agreement with the findings in Fig. 6c. This behaviour is in line with the observations in Fig. 6b. Finally, the influence of the roughness amplitude ϵ on the mean TPV is shown in Fig. 8c. This plot reveals that as ϵ increases the mean TPV of the particle in the transition region decreases. This is expected, as in the rough potential local barriers have to be overcome. This is exactly opposite to the effect of the noise intensity and the barrier height on the mean TPV of the rough inverted parabolic potential. For the numerical simulation of the mean TPV, we refer [41]. Next, we consider the change of the minimum mean TPV with barrier height k and noise intensity D for different roughness parameter ϵ as shown in Fig. 8d, e. It is found that $\min(\langle v(x) \rangle)$ increases with the increase in k or D. And with the increase in ϵ, the increasing trend is gradually slowing down. It can also be seen that the existence of a rough potential slows down the influence of barrier height and noise intensity on the mean TPV of the system.

We finally address the effect of varying the number n_b of sampling bins (i.e. changing the binning size) in our simulations. From a statistical analysis of the TPV in the interval $[-1, 1]$, we find that the behaviour of the mean TPV obtained by numerical simulation is fairly smooth for $n_b = 100$, as presented in Fig. 9a. For the case $n_b = 400$ in Fig. 9b, we need to increase the number of simulated trajectories to obtain the mean TPV. In this case, the shape of the mean TPV as function of the position x in the transition region shows increased roughness with visible local peaks. This effect is due to the finer sampling for larger n_b: while the smaller n_b averages over successive local maxima in the rough potential and thus leads to smoothening, the finer sampling retains the local variation. This expectation is corroborated in Fig. 9c, in which we see a direct correspondence of the variation of the mean TPV with the shape of the rough potential. Despite this effect in the shape of the mean TPV curve, the agreement with the theoretical prediction remains good.

4.4 Mean transition path shape

Our final point is the study of the mean transition path shape of the barrier crossing trajectories. We denote $\tau_{\text{shape}}^{\text{TP}}(x_0|x_A)$ and $\tau_{\text{shape}}^{\text{TP}}(x_0|x_B)$ as the mean transition path shapes from, respectively, the entry point x_A and the exit point x_B to the $x_0 \in [x_A, x_B]$. We focus on the influence of the roughness amplitude ϵ, the barrier shape factor k, and the noise intensity D. The symbols are the numerical results, and the solid and dashed lines are approximate theoretical results reported in Eqs. (18) and (19). We see that as x_0 gradually increases and approaches the exit point x_B, $\tau_{\text{shape}}^{\text{TP}}(x_0|x_A)$ shows an increasing trend, while simultaneously we see a decrease in $\tau_{\text{shape}}^{\text{TP}}(x_0|x_B)$. Figure 10a reveals that both $\tau_{\text{shape}}^{\text{TP}}(x_0|x_A)$ and $\tau_{\text{shape}}^{\text{TP}}(x_0|x_B)$ decrease with barrier shape factor k, in analogy to the observations for the mean TPT in Fig. 7. We also see the expected trends of the mean transition path shape for varying noise strength D and roughness amplitude ϵ in panels 10b and c. The agreement with the theoretical prediction (18) is very good. Similarly, we consider the change of the maximum value $\max(\tau_{\text{shape}}^{\text{TP}}(x_A|x_0))$ of the mean transition path shape with barrier height k and noise intensity D for different roughness parameter ϵ. It is found that $\max(\tau_{\text{shape}}^{\text{TP}}(x_A|x_0))$ decreases with the increase in k or D. And with the increase in ϵ, the decreasing trend is gradually
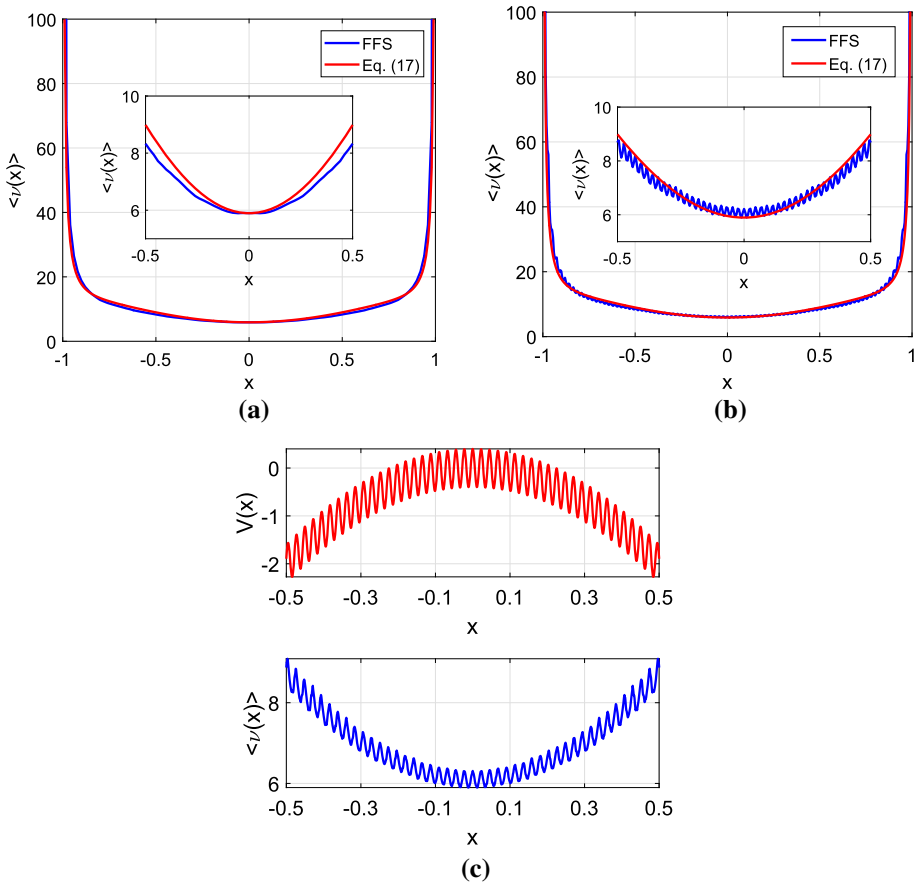
Fig. 9 Mean TPV as function of the position x in the transition region $[-1, 1]$, for $D = 1$, $k = 16$, $\epsilon = 0.4$, and $\omega = 279$. The number of sampling bins is taken as **a** $n_b = 100$ and **b** $n_b = 400$. For the finer sampling in **b**, the roughness of the potential is still visible, while it is smoothened out for the coarser sampling in **a**. The correspondence of the roughness of the mean TPV curve in **b** is shown to coincide with the variation of the rough barrier potential in panel **c**

intensifying. It also reveals that the rough potential function accelerates the effect of barrier height and noise intensity on the mean transition path shape.

5 Conclusions

We here analysed the representative quantities describing the thermally activated crossing of an inverted parabolic potential with superimposed roughness. Such models are actively studied for the description of transitions in complex systems, such as the conformational transitions occurring in the folding dynamics of proteins, or in reactions of biomolecules. The roughness reflects the complex effective energy landscape characteristic for such molecules. We studied in detail the mean TPT and the distribution of TPTs, along with the mean TPV and mean transition path shape of particles traversing this rough inverted parabolic potential. The
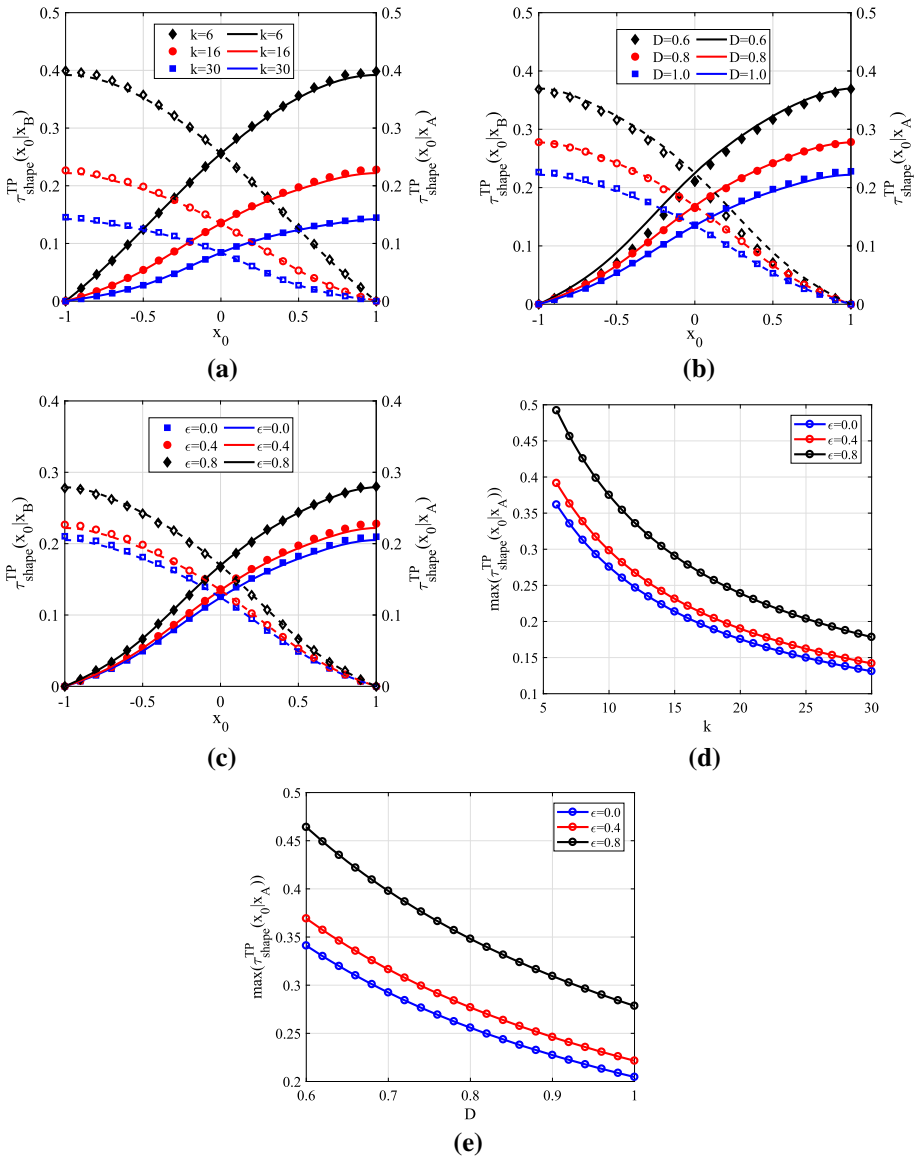
Fig. 10 Mean transition path shape as function of the reference point x_0 in the transition region $[-1, 1]$. The functional behaviour is shown for different **a** barrier shape factors k and $\epsilon = 0.4$, $D = 1$, $\omega = 279$; **b** noise strengths D and $k = 16$, $\epsilon = 0.4$, $\omega = 279$; **c** roughness amplitudes ϵ and $D = 1$, $k = 16$, $\omega = 279$. Symbols show results from simulations, the lines correspond to Eqs. (18) and (19). $\max(\langle \tau_{shape}^{TP}(x_A|x_0) \rangle)$ with different roughness amplitudes ϵ for **d** $D = 1.0$ and $\omega = 93$; **e** $k = 16$ and $\omega = 93$. In Fig. 10**d, e**, we show the theoretical results from Eq. (18)

correctness of the approximate theoretical results for the different quantities, derived from spatial averaging, was shown to agree very well with simulations obtained from the forward flux scheme. Specifically, we tested the effects of the barrier height, the roughness amplitude of the potential, and the noise intensity. It is well known that increased barrier heights lead to decreased TPTs and increased TPVs. This is attributed to the conditional character of these quantities, that solely take successful trajectories into account. This is in contrast to the first-passage time statistics. Here, both successful and unsuccessful trajectories are taken into consideration, such that, according to our intuition, higher barriers lead to longer first-passage times. With increasing roughness and decreasing noise intensity, both TPTs and first-passage times increase, while we observe an expected decrease in the TPVs. Analogous behaviours are observed for the transition path shapes. Moreover, the potential roughness accelerates the influence of barrier height and noise intensity on the mean TPT and the mean transition path shape. Furthermore, to a certain extent, the influence of barrier height and noise intensity on the mean TPV is reduced. Finally, we also studied the influence of the binning size on the mean TPV and showed how a sufficiently small bin size reveals the rough nature of the underlying potential barrier.

While the general agreement of the simulations results with the approximate theoretical description was good in all cases, some deviations were observed to grow with increasing roughness of the potential, or for low barriers. It will be a task for future work to find ways to improve the approximations in the theoretical framework for rough potentials. Moreover, it will be of interest to consider non-Gaussian types of noise, such as white Lévy stable noise, for which an extensive mathematical framework exists for first-passage time statistics [77–79]. Similarly, different Gaussian noise sources should be studied, such as coloured, Poissonian, or long-range correlated noise.

Appendix A: The transition path probability density function

According to Eq. (1), the reactive trajectories from x_A to x_B should satisfy the stochastic differential equation [21]

$$dx = \left(f(x) + \frac{2D \, d\phi_B(x)/dx}{\phi_B(x)} \right) dt + \sqrt{2D} \, dW(t), \qquad (A1)$$

where $W(t)$ is the unit Wiener process, $\phi_B(x)$ is the committor function as shown in Eq. (11). Then, the probability density function for the transition paths, $P_{TP}(x, t)$ from x_A to x_B, satisfies

$$\frac{\partial P_{TP}(x,t)}{\partial t} = -\frac{\partial}{\partial x} \left(f(x) + \frac{2D \, d\phi_B(x)/dx}{\phi_B(x)} \right) P_{TP}(x,t) + D\frac{\partial^2}{\partial x^2} P_{TP}(x,t). \quad (A2)$$

With $f(x) = -dV(x)/dx = -(1/D)dG(x)/dx$,

$$\frac{\partial P_{TP}(x,t)}{\partial t} = \frac{\partial}{\partial x} \left(D \left[\frac{1}{D^2} \frac{dG(x)}{dx} - \frac{2d\phi_B(x)/dx}{\phi_B(x)} + \frac{\partial}{\partial x} \right] P_{TP}(x,t) \right). \qquad (A3)$$

Defining $M(x) = \exp(G(x)/D)$, we obtain

$$\frac{\partial P_{\text{TP}}(x,t)}{\partial t} = \frac{\partial}{\partial x} \left(\frac{D\phi_{\text{B}}^2(x)}{M(x)} \left[\frac{M(x)D^{-1}dM(x)/\mathrm{d}x}{\phi_{\text{B}}^2(x)} \right. \right.$$
$$\left. \left. - \frac{2M(x)(\mathrm{d}\phi_{\text{B}}(x)/\mathrm{d}x)\phi_{\text{B}}(x)}{\phi_{\text{B}}^4(x)} + \frac{M(x)}{\phi_{\text{B}}^2(x)} \frac{\partial}{\partial x} \right) P_{\text{TP}}(x,t) \right). \quad (A4)$$

Hence, Eq. (A2) is recast in the Smoluchowski equation [72].

$$\frac{\partial P_{\text{TP}}(x,t)}{\partial t} = \frac{\partial}{\partial x} \left(D\phi_{\text{B}}^2(x) \exp\left(-\frac{G(x)}{D}\right) \frac{\partial}{\partial x} \frac{\exp(G(x)/D)}{\phi_{\text{B}}^2(x)} P_{\text{TP}}(x,t) \right). \quad (A5)$$

This is Eq. (9) in the main text.

References

1. E. Pollak, P. Talkner, Chaos **15**, 026116 (2005)
2. S. Arrhenius, Z. Phys, Chem. (Leipzig) **4**, 216 (1889)
3. H. Eyring, J. Chem. Phys. **3**, 107 (1935)
4. B.C. Garrett, Theor. Chem. Acc. **103**, 200 (2000)
5. E. Wigner, Trans. Faraday Soc. **34**, 29 (1938)
6. G.A. Petersson, Theor. Chem. Acc. **103**, 190 (1995)
7. H.A. Kramers, Physica **7**, 284 (1940)
8. A. Einstein, Ann. Phys. (Leipzig) **322**, 549 (1905)
9. M. Smoluchowski, Ann. Phys. (Leipzig) **21**, 756 (1906)
10. P. Hänggi, P. Talkner, M. Borkovec, Rev. Mod. Phys. **62**, 251 (1990)
11. H.S. Chung, K. McHale, J.M. Louis, W.A. Eaton, Science **335**, 981 (2012)
12. H.S. Chung, W.A. Eaton, Nature **502**, 685 (2013)
13. H.S. Chung, S. Piana-Agostinetti, D.E. Shaw, W.A. Eaton, Science **349**, 1504 (2015)
14. K. Neupane, A.P. Manuel, M.T. Woodside, Nat. Phys. **12**, 700 (2016)
15. F. Sturzenegger, F. Zosel, E.D. Holmstrom, K.J. Buholzer, D.E. Makarov, D. Nettels, B. Schuler, Nat. Commun. **9**, 4708 (2018)
16. K. Neupane, D.A.N. Foster, D.R. Dee, H. Yu, F. Wang, M.T. Woodside, Science **352**, 239 (2016)
17. P. Cossio, G. Hummer, A. Szabo, J. Chem. Phys. **148**, 123309 (2018)
18. D.E. Makarov, J. Chem. Phys. **143**, 194103 (2015)
19. D. Chandler, J. Chem. Phys. **68**, 2959 (1978)
20. C. Dellago, P.G. Bolhuis, D. Chandler, J. Chem. Phys. **108**, 9236 (1998)
21. J.F. Lu, J. Nolen, Probab. Theory Rel. **161**, 195 (2015)
22. A.T. Hawk, S.S.M. Konda, D.E. Makarov, J. Chem. Phys. **139**, 064101 (2013)
23. C. Dellago, P.G. Bolhuis, P.L. Geissler, Adv. Chem. Phys. **123**, 1 (2002)
24. P.G. Bolhuis, D. Chandler, C. Dellago, P.L. Geissler, Ann. Rev. Phys. Chem. **53**, 291 (2002)
25. A.M. Berezhkovskii, G. Hummer, S.M. Bezrukov, Phys. Rev. Lett. **97**, 020601 (2006)
26. N. Krishna, Phys. Rev. Lett. **109**, 068102 (2012)
27. H.S. Chung, W.A. Eaton, Curr. Opin. Struct. Biol. **48**, 30 (2018)
28. K. Neupane, A.P. Manuel, J. Lambert, M.T. Woodside, J. Phys. Chem. Lett. **6**, 1005 (2015)
29. N.Q. Hoffer, M.T. Woodside, Curr. Opin. Struct. Biol. **53**, 68 (2019)
30. P.C. Bressloff, S.D. Lawley, J. Phys. A Math. Theor. **48**, 225001 (2015)
31. A. Godec, R. Metzler, Sci. Rep. **6**, 20349 (2016)
32. A. Godec, R. Metzler, Phys. Rev. X **6**, 041037 (2016)
33. A. Godec, R. Metzler, J. Phys. A **50**, 084001 (2017)
34. O. Pulkkinen, R. Metzler, Phys. Rev. Lett. **110**, 198101 (2013)
35. D. Grebenkov, R. Metzler, G. Oshanin, Phys. Chem. Chem. Phys. **20**, 16393 (2018)
36. D. Grebenkov, R. Metzler, G. Oshanin, Commun. Chem. **1**, 96 (2018)
37. D. Grebenkov, R. Metzler, G. Oshanin, New J. Phys. **21**, 122001 (2019)
38. Y. Xu, H. Li, H.Y. Wang, W.T. Jia, X.L. Yue, J. Kurths, J. Appl. Mech. Trans. ASME **84**, 091004 (2017)
39. A.M. Berezhkovskii, L. Dagdug, S.M. Bezrukov, J. Phys. Chem. B **121**, 5455 (2017)

40. J. Deepika, J. Phys. A Math. Theor. **51**, 285001 (2018)
41. A.M. Berezhkovskii, D.E. Makarov, J. Chem. Phys. **148**, 201102 (2018)
42. N.Q. Hoffer, K. Neupane, A.G.T. Pyo, M.T. Woodside, Proc. Natl. Acad. Sci. USA **116**, 8125 (2019)
43. H. Yu, A.N. Gupta, X. Liu, K. Neupane, A.M. Btigley, I. Sosova, M.T. Woodside, Proc. Natl. Acad. Sci. USA **109**, 14452 (2012)
44. M. Laleman, E. Carlon, H. Orland, J. Chem. Phys. **147**, 214103 (2017)
45. E. Pollak, Phys. Chem. Chem. Phys. **18**, 28872 (2016)
46. A.M. Berezhkovskii, L. Dagdug, S.M. Bezrukov, J. Phys. Chem. B **123**, 3786 (2019)
47. W.K. Kim, R.R. Netz, J. Chem. Phys. **143**, 224108 (2015)
48. H.S. Chung, I.V. Gopich, Phys. Chem. Chem. Phys. **16**, 18644 (2014)
49. E. Medina, R. Satija, D.E. Makarov, J. Phys. Chem. B **122**, 11400 (2018)
50. R. Satija, D.E. Makarov, J. Phys. Chem. B **123**, 802 (2019)
51. R. Satija, A. Das, D.E. Makarov, J. Chem. Phys. **147**, 152707 (2017)
52. E. Carlon, H. Orland, T. Sakaue, C. Vanderzande, J. Phys. Chem. B **122**, 11186 (2018)
53. J. Gladrow, R. Crivellari, F. Ritort, U.F. Keyser, Nat. Commun. **10**, 55 (2019)
54. H. Janovjak, H. Knaus, D.J. Muller, J. Am. Chem. Soc. **129**, 246 (2007)
55. P. Scheidler, W. Kob, K. Binder, J. Phys. Chem. B **108**, 6673 (2004)
56. T.S. Chow, Phys. Lett. A **342**, 148 (2005)
57. J. Wang, J. Onuchic, P. Wolynes, Phys. Rev. Lett. **76**, 4861 (1996)
58. R. Zwanzig, Proc. Natl. Acad. Sci. USA **85**, 2029 (1998)
59. Y.G. Li, Y. Xu, J. Kurths, X.L. Yue, Chaos **27**, 103102 (2017)
60. Y.G. Li, Y. Xu, J. Kurths, Phys. Rev. E **96**, 052121 (2017)
61. Y.G. Li, Y. Xu, J. Kurths, X.L. Yue, Phys. Rev. E **94**, 042222 (2016)
62. Y.G. Li, Y. Xu, J. Kurths, Phys. Rev. E **99**, 052203 (2019)
63. M. Hu, J.D. Bao, Phys. Rev. E **97**, 062143 (2018)
64. Y.G. Li, Y. Xu, J. Kurths, J.Q. Duan, Chaos **29**, 101102 (2019)
65. D. Mondal, P.K. Ghosh, D.S. Ray, J. Chem. Phys. **130**, 074703 (2009)
66. H. Li, Y. Xu, J. Kurths, X.L. Yue, Eur. Phys. J. B **92**, 76 (2019)
67. R.J. Allen, P.B. Warren, P.R.T. Wolde, Phys. Rev. Lett. **94**, 018104 (2005)
68. H. Risken, *The Fokker–Planck Equation: Methods of Solution and Applications* (Springer, Berlin, 1996)
69. B.W. Zhang, D. Jasnow, J. Chem. Phys. **126**, 074504 (2007)
70. B.G. Wenslwy, S. Batey, F.A.C. Bone, Z.M. Chan, N.R. Tumelty, A. Steward, L.G. Kwa, A. Borgia, J. Clarke, Nature **463**, 685 (2010)
71. G. Hummer, J. Chem. Phys. **120**, 516 (2004)
72. A.G.T. Pyo, N.Q. Hoffer, K. Neupane, M.T. Woodside, J. Chem. Phys. **149**, 115101 (2018)
73. C.W. Gardiner, *Handbook of Stochastic Methods* (Springer, Berlin, 1985)
74. V.V. Palyulin, R. Metzler, J. Stat. Mech. **2012**, L03001 (2012)
75. V.V. Palyulin, R. Metzler, J. Phys. A **47**, 032002 (2014)
76. T. Mattos, C. Mejía-Monasterio, R. Metzler, G. Oshanin, Phys. Rev. E **86**, 031143 (2012)
77. V.V. Palyulin, A.V. Chechkin, R. Metzler, Proc. Natl. Acad. Sci. USA **111**, 2931 (2014)
78. V.V. Palyulin, A.V. Chechkin, R. Klages, R. Metzler, J. Phys. A **49**, 394002 (2016)
79. V.V. Palyulin, G. Blackburn, M.A. Lomholt, N. Watkins, R. Metzler, R. Klages, A.V. Chechkin, New J. Phys. **21**, 103028 (2019)